Effect of Electrode Material on Sensing Performance of MEMS-based Pyroelectric Sensors

Zhen Xiong, Chia-Yu Tsai, and Chia-Yen Lee[*]

Department of Materials Engineering, National Pingtung University of Science and Technology,
Pingtung 912, Taiwan

MEMS technology is employed to fabricate human infrared sensors on double-sided polished glass substrates. For each device, the sensing layer consists of a thin ZnO film deposited on the lower electrode by RF magnetron sputtering. The top electrode was deposited by an electron beam evaporation method with the same material as that used for the bottom electrode. Numerical and experimental investigations were performed to examine the effects of five different electrode materials (Cr, Cu, Au, Pt, and Ag) on the sensing performance of the fabricated device. The experimental results showed that the use of Ag as the electrode material results in the highest response voltage (23 mV/mW) at a chopping frequency of 60 Hz. Additionally, the simulation results showed that the Ag electrodes yield the fastest temperature response. For all the electrode materials, the temperature-time change rate of the sensing layer was positively correlated with the voltage response of the sensor chip.

1. Introduction

MEMS-based pyroelectric infrared sensors, consisting of a thin film of ferroelectric crystal material sandwiched between two electrodes, produce an electrical voltage (or current) in response to temperature variation and have found widespread use in recent years for many applications, including fire detection, intruder alarms, and infrared light detection, as well as imaging, body temperature monitoring, respiration, and heart rate detection, and so on. Moreover, pyroelectric sensors can be easily integrated with modern IC circuits to create sophisticated system-on-chip (SoC) devices for a wide variety of sensing and detection applications.[1,2]

Among pyroelectric materials, zinc oxide (ZnO) is a multifunctional material with many favorable properties, including excellent photoconductivity, piezoelectricity, pyroelectricity, and acousticoptical characteristics.[3] The crystal structure of ZnO is mainly composed of hexagonal wurtzite and cubic zinc-blende phases. Both phases have piezoelectric effects due to their symmetry, while the wurtzite structure also has pyroelectric properties. Thus, ZnO is an attractive material for precise and responsive temperature measurement and control. Hashimoto

et al.[4] developed a pyroelectric array detector for determining the direction and number of individuals passing through a doorway. The detector operated with a supply voltage of 5 V and incorporated a thin $PbTiO_3$ bulk ceramic film with a thickness of approximately 40 μm. The device exhibited a peak voltage sensitivity of 23 mV/mW at a chopping frequency of 10 Hz. Lienhard *et al.*[5] investigated the transmittance properties of thin nickel (Ni) films deposited on pyroelectric polyvinylidene fluoride (PVDF) substrates at infrared wavelengths ranging from 2 to 50 μm. The results revealed that even slight variations in film thickness had a substantial impact on the absorbance characteristics of the sensor. Chang and Tang[6] fabricated an integrated pyroelectric sensor comprising a PZT thin film and a Si junction gate field-effect transistor (JFET). The performance of the sensor was evaluated at a modulation frequency spectrum from 0.2 to 10 Hz. The device showed a voltage sensitivity of 191 mV/mW at a modulation frequency of 1 Hz for a Si substrate of 500 μm thickness. Lienhard *et al.*[1] deposited a thin Ni layer on the surface of a lead zirconate titanate (PZT) pyroelectric sensor to serve as both the top electrode and a selective absorption layer. The resulting sensor exhibited peak absorption coefficients of 0.8 at a wavelength of 0.664 μm and 0.7 at a wavelength of 4 μm.

Ko *et al.*[7] fabricated a MEMS-based IR sensor consisting of a PZT sensing film, gold upper electrodes, platinum lower electrodes, and a double-sided polished silicon wafer substrate. The sensor performance was investigated for four different designs: (1) membrane–substrate-patterned-Pt, (2) membrane–substrate-no-patterned-Pt, (3) silicon–substrate-patterned-Pt, and (4) silicon–substrate-no-patterned-Pt. The use of a membrane design resulted in both an improved current response and a faster response. Chong *et al.*[8] constructed a thin-film pyroelectric sensor array comprising 16 sensing elements composed of metal–ZnO–metal sandwiched layers, each measuring 200 μm in length and width. By placing the sensing elements on a thermally isolated and self-supporting Si_3N_4/SiO_2 membrane with a cut-off frequency of 20 Hz, the sensor performance was improved to a maximum voltage sensitivity of approximately 110 mV/mW. Wei *et al.*[9] developed a pyroelectric sensor incorporating a Si_3N_4 thin film as the membrane and thermal isolation layer and a (100) silicon wafer as the substrate. A thin ZnO layer was used as the sensing layer, and Au/Cr layers with thicknesses of 100 nm/10 nm were employed as both the upper and lower electrodes. Three sets of sensors were fabricated and characterized, with each sensor having a different layer thickness, effective sensing area, and electrode coverage (i.e., partially and fully covered electrodes). It was found that, for a given sensor area and ZnO thickness, the voltage responsivity improved as the top electrode coverage decreased.

In 2009, Hsiao *et al.*[10] investigated the residual stress and mechanical properties of a ZnO multilayer film stack. The analyses considered three ZnO layers, each with a total thickness of 450 nm, deposited by RF sputtering at different RF powers (90 , 120, and 150 W). The best morphology and mechanical properties were obtained for the film deposited at 120 W. Hsiao and Yu[11] developed different pyroelectric sensor electrode layouts to enhance the film's voltage responsivity. In their experiments, the proposed layout with an array-type configuration yielded signals about 3.6 times higher than those of fully covered ones and 2 times higher than those of partially covered ones in ZnO-based pyroelectric sensors. Additionally, the finite element modeling demonstrated that partially covered electrodes improved temperature variation rates in the ZnO layer.

Cicek *et al.*[12] utilized RF and DC magnetron sputtering techniques to deposit ZnO thin films on silicon and porous silicon (PS) substrates. The PS substrate had a larger internal surface area, lower thermal conductivity, and c-axis orientation. It therefore achieved a high pyroelectric coefficient of 8.2, representing a 400-fold improvement over that obtained with the silicon substrate. Gaur *et al.*[13] introduced a pyroelectric detector that featured a polycrystalline AlN thin film coupled with a 1.0-μm-thick SiO_2 layer, serving both as a thermal isolation barrier and a diaphragm to support the sensor structure. They demonstrated that the device's absorptive properties could be enhanced by sputtering an additional 160-nm-thick Au film onto the AlN layer. Through characterization, it was determined that the device exhibited a response time of 8.0 ms and a pyroelectric current responsivity of 2.5×10^{-6} A/W. In 2021, Lee *et al.*[14] fabricated pyroelectric infrared sensors with suspended ZnO pyroelectric films and thermally insulated Si substrates using thin-film deposition, photolithography, and etching techniques. The responsivity of the pyroelectric films was improved by annealing them at 500 °C for 4 h. The experimental results showed a strong correlation between the peak intensity of the sensing film in the (002) crystal orientation and the voltage response of the device. The temperature variation and voltage responsivity of the fabricated sensors were evaluated for substrate thicknesses ranging from 1 to 500 μm. The temperature variation and voltage responsivity both increased with decreasing substrate thickness. For the lowest film thickness of 1 μm, the sensor showed a voltage sensitivity of 3880 mV/mW at a cutoff frequency of 400 Hz. Sharmila *et al.*[15] examined the effects of the annealing temperature (100–300 °C) on the morphological, structural, and optical properties of ZnO thin films. The films annealed at 200 and 300 °C showed a photo-to-dark current ratio (PDCR) around 100 times higher than that of the film annealed at 100 °C. Bozoian *et al.*[16] investigated the infrared reflectivity of ZnO thin films deposited on glass substrates via pulsed laser deposition at 350 and 700 °C at different deposition times. Their experimental results showed that film thickness significantly affects dielectric constants and oscillator damping factors. It is clear that the ZnO thin films exhibit high carrier densities at a deposition temperature of 350 °C and thicknesses of 110–150 nm. The deposition parameters of the ZnO thin film were found to be important factors for infrared sensor performance.

In the previous research studies, many sensing materials and sensor designs of pyroelectric sensors were studied, but there are only few ones investigating the effects of the electrode material on the pyroelectric properties of ZnO. The objective of this research is to enhance the performance of human-infrared-sensing thin films by process and material selection. In this study, we employed MEMS technology to fabricate human infrared sensors on double-sided polished glass substrates. Numerical and experimental investigations were performed to examine the effects of five different electrode materials (Cr, Cu, Au, Pt, and Ag) on the sensing performance of the fabricated device. The results showed that optimal sensing performance is obtained using Ag as the electrode material.

2.   Materials and Principles

Pyroelectric materials generate an electric charge when exposed to changes in temperature and are thus often used as infrared sensing elements. The basic structure of an infrared sensor is

shown in Fig. 1, where the electrode has a surface area of A and the pyroelectric layer has a thickness of d. Assuming that the ambient temperature is T and the sensor is irradiated by infrared rays, the radiation power $W(t)$ is given by[17]

$$W(t) = W_0 e^{iwt}, \tag{1}$$

where W_0 is the infrared input power and ω is the chopping frequency.

The IR power acquired by the sensor, denoted as $\eta W(t)$, can be obtained using the following heat transfer equation:[17]

$$\eta W(t) = H_T \frac{d\delta}{dt} + G_T \delta . \tag{2}$$

The temperature difference is represented by δ, the radiation absorption rate is represented by η, H_T is the heat volume ($J \div K$), G_T is the thermal conductivity coefficient ($W \div K$), and the time constant is $\tau_T = HT \div GT$, which can be obtained by solving Eq. (2). δ is shown in the following equation:[17]

$$\delta = \frac{\eta W_0 e^{\square}}{G_T + iwH_T} . \tag{3}$$

By differentiating Eq. (3), the temperature-time change rate $d\delta \div dt$ is obtained as

$$\frac{d\delta}{dt} = \frac{\omega \eta W_0}{G_T \left(1 + \omega^2 \tau_T^2\right)^{\frac{1}{2}}}. \tag{4}$$

Owing to the change in the surface temperature induced by the received thermal radiation, the pyroelectric layer spontaneously polarizes, generating a pyroelectric change rate ΔPs, which
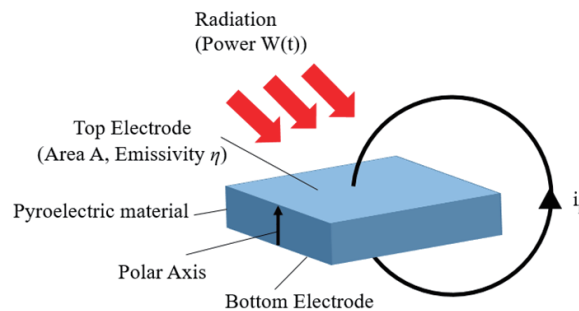

Fig. 1. (Color online) Pyroelectric effect.[14]

causes a charge Q to be produced on the surface in accordance with[17]

$$Q = A \times \Delta P_s. \tag{5}$$

Following a manipulation process, ΔPs can be expressed as[17]

$$\Delta P_s = p \times \Delta \delta , \tag{6}$$

where p is the pyroelectric coefficient, A is the area of the top electrode that overlaps the pyroelectric layer, and $\Delta \delta$ is the temperature change. The resulting pyroelectric current i_p can then be obtained as[17]

$$i_p = A \times \frac{dP_s}{dt} = Ap' \times \frac{d\delta}{dt} , \tag{7}$$

where p' is the vertical component of p when it passes through the electrode surface.

3.   Methods and Fabrication

The performance of the ZnO infrared sensor was evaluated both numerically and experimentally.

3.1   Simulation method

ANSYS FLUENT software was used to construct a static heat transfer model of the sensor. The model was simplified to a 3/4 cross-sectional view and used to investigate the effect of the electrode material on the temperature variation rate of the sensor when exposed to a human heat source. The model was meshed using a uniform grid of rectangular elements. Owing to the irregular shape of the sensor, the model was divided into four separate meshes, A, B, C, and D, for computational expediency. The material properties of the electrodes and substrate were assigned the values shown in Table 1. Finally, a 36 °C heat source was applied to the top electrode as the boundary condition for temperature conduction analysis.

Figure 2(a) shows the general region of the sensor considered in the simulation process. Figure 2(b) provides a detailed view, where individual simulation points are divided into four groups located in different areas of the sensor. Specifically, Area A is located on the central plane of the sensing layer and lies beneath the upper electrode. Area B is located on the same plane but lies in the exposed region of the sensing layer. Areas C and D are located directly beneath Areas A and B, respectively, and lie at the interface between the sensing layer and the bottom electrode.

Table 1
Material parameters used in simulation analysis.

Electrode material	Thermal conductivity (W/mk)	Density (kg/m^3)	Specific heat (j/kg-k)
Ag	420	10490	230
Au	318	19320	130
Pt	70	21090	130
Cu	401	8920	390
Cr	93	7190	449
ZnO	110	5610	520
Glass Substrate	0.74	2700	750
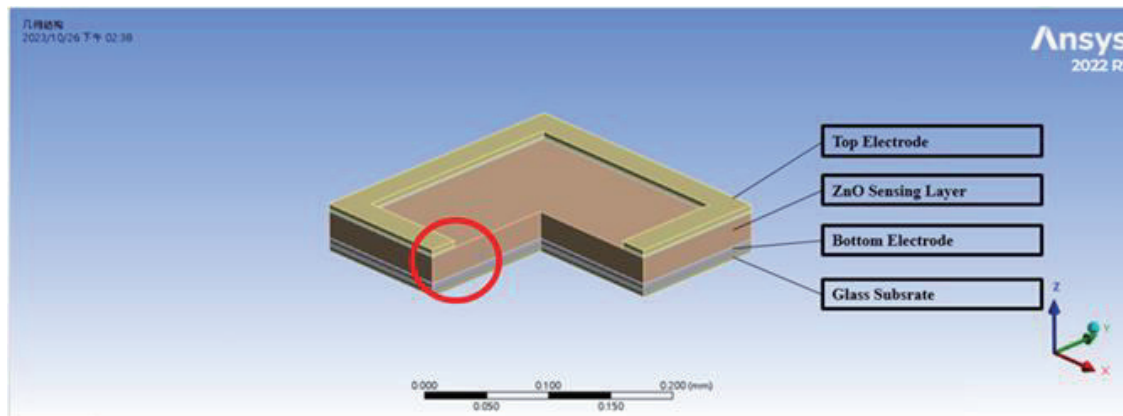
(a)
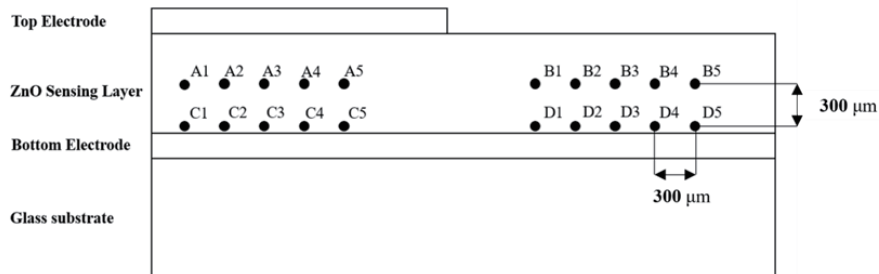
(b)

Fig. 2.   (Color online) (a) ANSYS simulation region and (b) detailed locations of simulation points considered in analysis.

3.2   Fabrication

Figure 3 shows the basic structure and dimensions of the proposed ZnO sensor. Figure 4 illustrates the main steps involved in the fabrication process. The process began by depositing the bottom electrode on a double-sided polished glass substrate using electron beam evaporation with the chosen metallic material (electron gun power rate: 2.2%; pressure: 5 mTorr; deposition

(a)

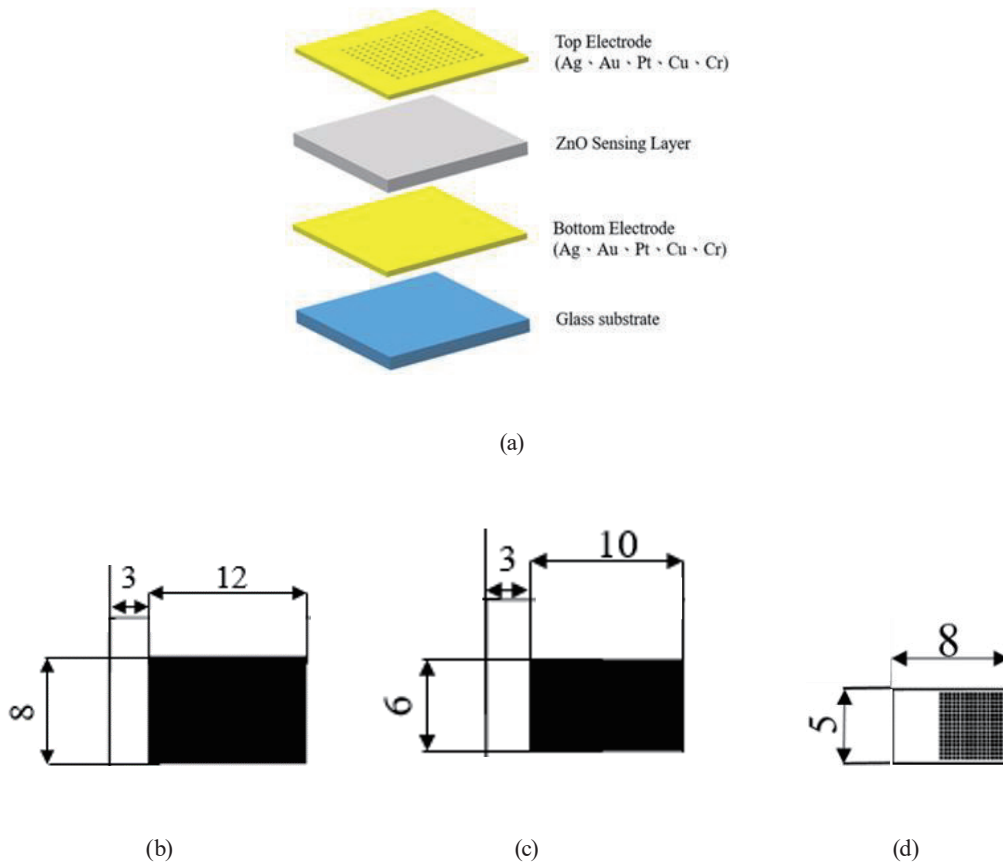(b)   (c)   (d)

Fig. 3.   (Color online) Design of MEMS-based pyroelectric infrared sensor. (a) Structural arrangement of sensor and dimensions of (b) bottom electrode, (c) sensing layer, and (d) top electrode with a grid side length of 200 μm and 16 × 16 electrode units (units: mm).
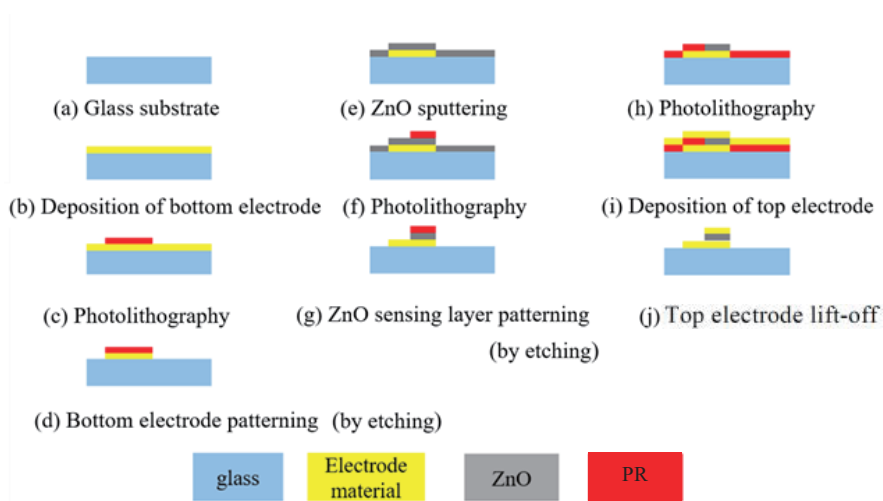

Fig. 4.   (Color online) Schematic illustration showing main steps in fabrication of pyroelectric infrared sensor: Process 1 – deposition of bottom electrodes; Process 2 – deposition of ZnO sensing layer and Process 3 – deposition of top electrodes.

rate: 0.5 Å/s). The bottom electrode was patterned using a standard photolithography method, and the ZnO sensing layer was then deposited on the electrode by radio-frequency magnetron sputtering (sputtering power: 150 W, Ar flow rate: 30 sccm, pressure: 5 mTorr, substrate temperature: 170 °C, time: 2.5 h). The as-deposited thickness of the ZnO layer is 595 nm. Finally, the top electrode, consisting of the same material as that used for the lower electrode, was deposited by electron beam evaporation and patterned using a metal lift-off technique to define a dense grid pattern with a grid side length of 200 μm and 256 electrode units. The thicknesses of the electrodes and adhesion layers are listed in Table 2. Figure 5 shows a photograph of the completed chip after the fabrication processes.

4. Results and Discussion

Figures 6(a) and 6(b) show the average simulated temperature responses at points A1–A5 and B1–B5, respectively, given the application of the IR heat source to the upper sensor surface. In both regions, the response time varied significantly with changes in the material used to fabricate the electrodes. In particular, the Ag electrode exhibited the fastest temperature response, with the time required to reach 90% of the final response approximately 9% lower than that of the Cr electrode with the slowest temperature response. The similar temperature trends in the two areas indicate that the sensing layer provided a uniform response, irrespective of the top electrode coverage. Figures 6(c) and 6(d) show the equivalent results for Areas C and D of the sensor, respectively. The effect of the electrode material on the temperature response was similar to that observed in Areas A and B. In Area C, the Ag electrode reduced the t_{90} time

Table 2
Electrode material and thickness (total thickness of individual electrodes: 1550 Å).

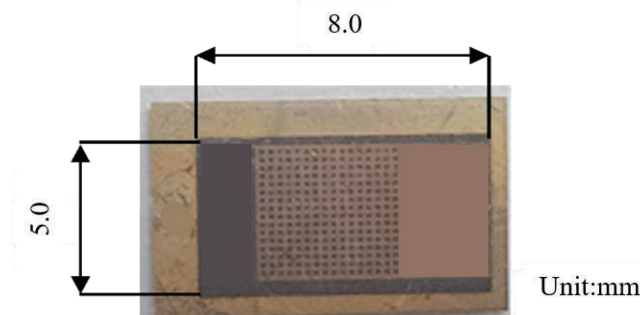| Electrode material	Adhesion layer
Ag 1200 Å	Cr 350 Å
Au 1200 Å	Cr 350 Å
Pt 1200 Å	Cr 350 Å
Cu 1550 Å	X
Cr 1550 Å	X

Fig. 5. (Color online) Photograph of completed chip after fabrication processes.
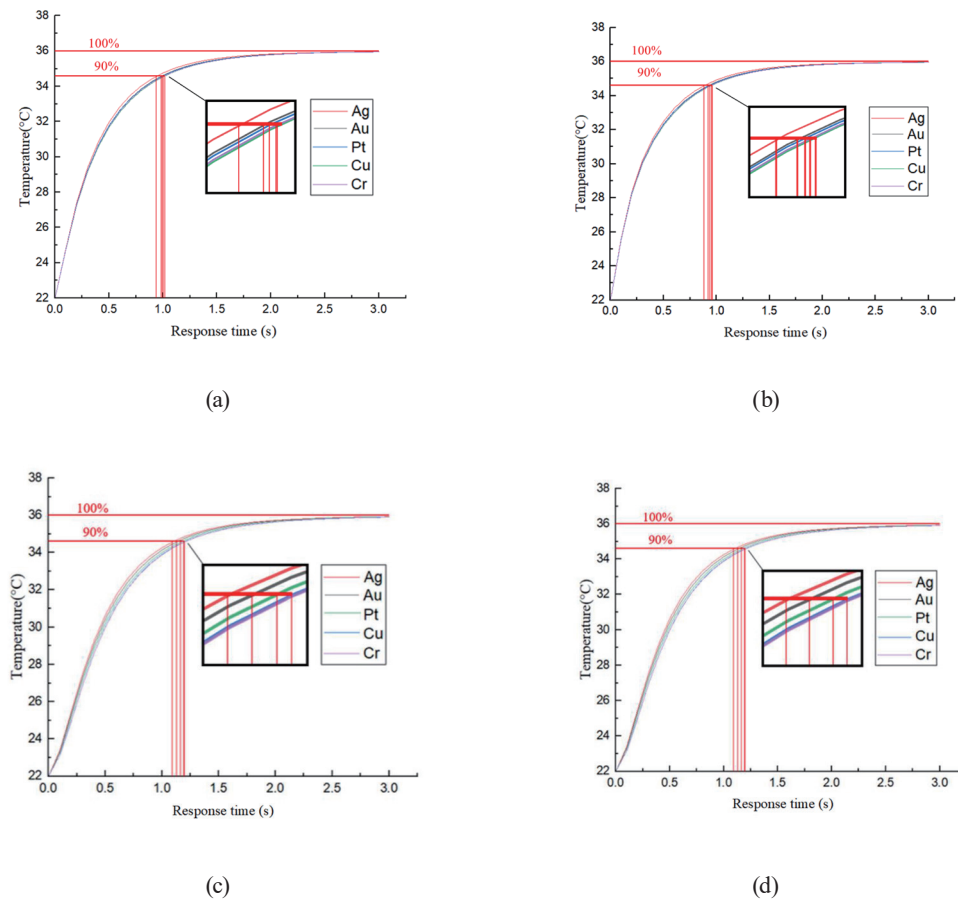
Fig. 6.   (Color online) Average temperature-time change rate curves for different electrode materials in different areas: (a) Area A, (b) Area B, (c) Area C, and (d) Area D.

by 18% compared with the Cr electrode. The t_{90} values of the different electrode materials in Area D were identical to those in Area C. Hence, it was inferred that the lower edge of the sensing layer was under temperature equilibrium conditions. In other words, the temperature response of the lower region of the sensing layer was dominated by the electrode material rather than the coverage of the sensing area. Table 3 shows the average temperature-time change rates in Areas A–D for each electrode material. Overall, the results presented in Fig. 6 and Table 3 show that the effects of the electrode material on the t_{90} temperature-time response can be ranked in descending order as Ag > Au > Pt > Cu > Cr. Moreover, the similar t_{90} temperature-time change rates observed in Areas C and D for the different electrode materials suggest that the thermal conductivity of the bottom electrode layer has only a minimal effect on the overall response of the chip.

Figure 7 shows the main components of the experimental system used to evaluate the performance of the sensors fabricated using different electrode materials. The heat source was provided by an infrared laser with a power of 10 mW and a wavelength of 765 nm. The laser spot was expanded to a diameter of 3 mm using a beam expander. In addition, an X-Y translation

Table 3
t_{90} temperature-time change rates in different areas of sensor for different electrode materials.

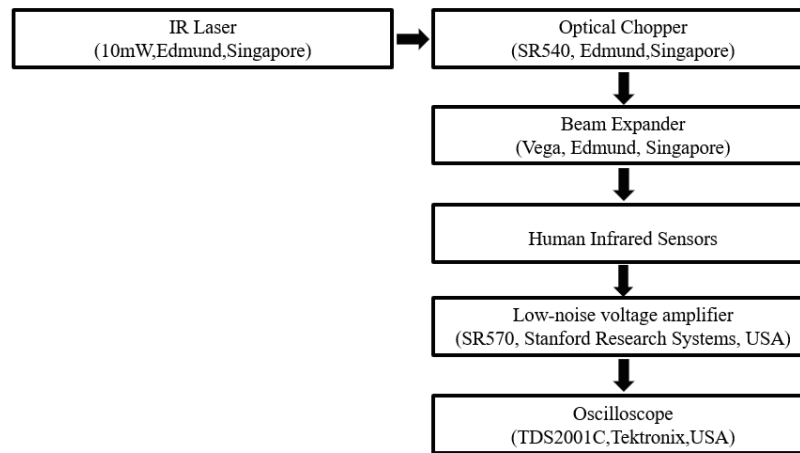| Electrode material	Area A, t_{90} (s)	Area B, t_{90} (s)	Area C, t_{90} (s)	Area D, t_{90} (s)
Ag/Cr	0.935	0.88	1.08	1.08
Au/Cr	0.98	0.92	1.13	1.13
Pt	0.99	0.935	1.165	1.165
Cu	1.00	0.953	1.195	1.195
Cr	1.015	0.96	1.195	1.195

Fig. 7.　Main components of experimental measurement platform.

stage was employed to adjust the position of the sensor such that the aperture could be focused on the entire sensor surface. The distance between the heat source and the sensor was set at 30 cm. The sensor was connected to an SR570 low-noise voltage amplifier via an SMA connector. The amplified signal was displayed on an oscilloscope and used to measure the voltage response of the infrared heat source at different chopping frequencies.

The ZnO thin films were deposited on the lower electrodes using an argon sputtering process and then annealed at 300, 400, and 500 °C for 4 h. The microstructures of the annealed films were examined by X-ray diffraction (XRD) using a Cu target (Monochromatic Cu-Kα, $\lambda = 0.154$ nm) as the excitation source. The XRD patterns were acquired at an operating voltage of 40 kV and a current of 40 mA. The scanning range was set as 30–60° with a sampling interval of 0.03° and a sampling time of 0.45 s. The XRD patterns of the annealed films are shown in Fig. 8, along with that of a nonannealed film. The intensity of the (002) peak increased following annealing and reached a maximum value in the sample annealed at the highest temperature of 500 °C.

Figure 9 shows the SEM surface morphologies of the ZnO films processed at different annealing temperatures. As shown in Fig. 9(a), the as-deposited film had a relatively loose morphology consisting of small spherical structures with clear grain boundaries. After annealing at 300 °C for 4 h, the grain size increased, and some of the spherical structures transformed into large lamellar structures [Fig. 9(b)]. When the annealing temperature was increased to 400 °C,
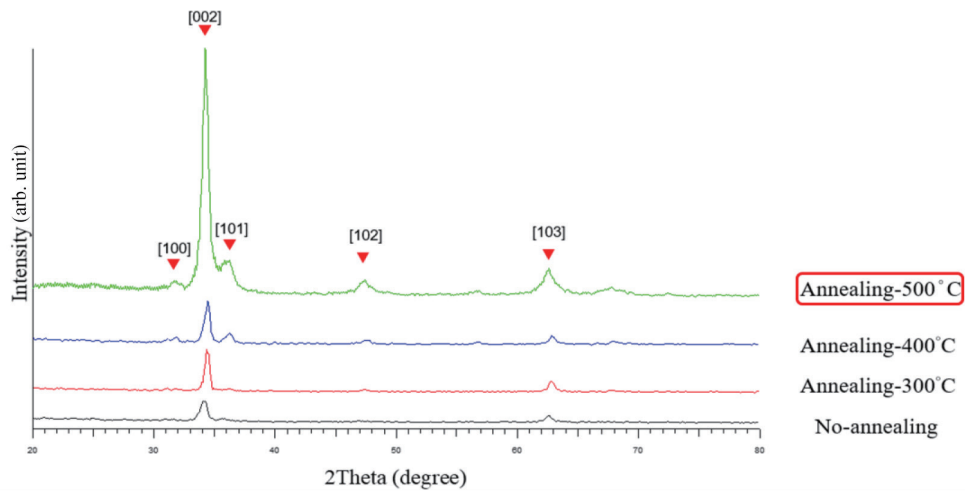
Fig. 8. (Color online) XRD patterns of ZnO films sputtered at different annealing temperatures (300, 400, and 500 ºC for 4 h).
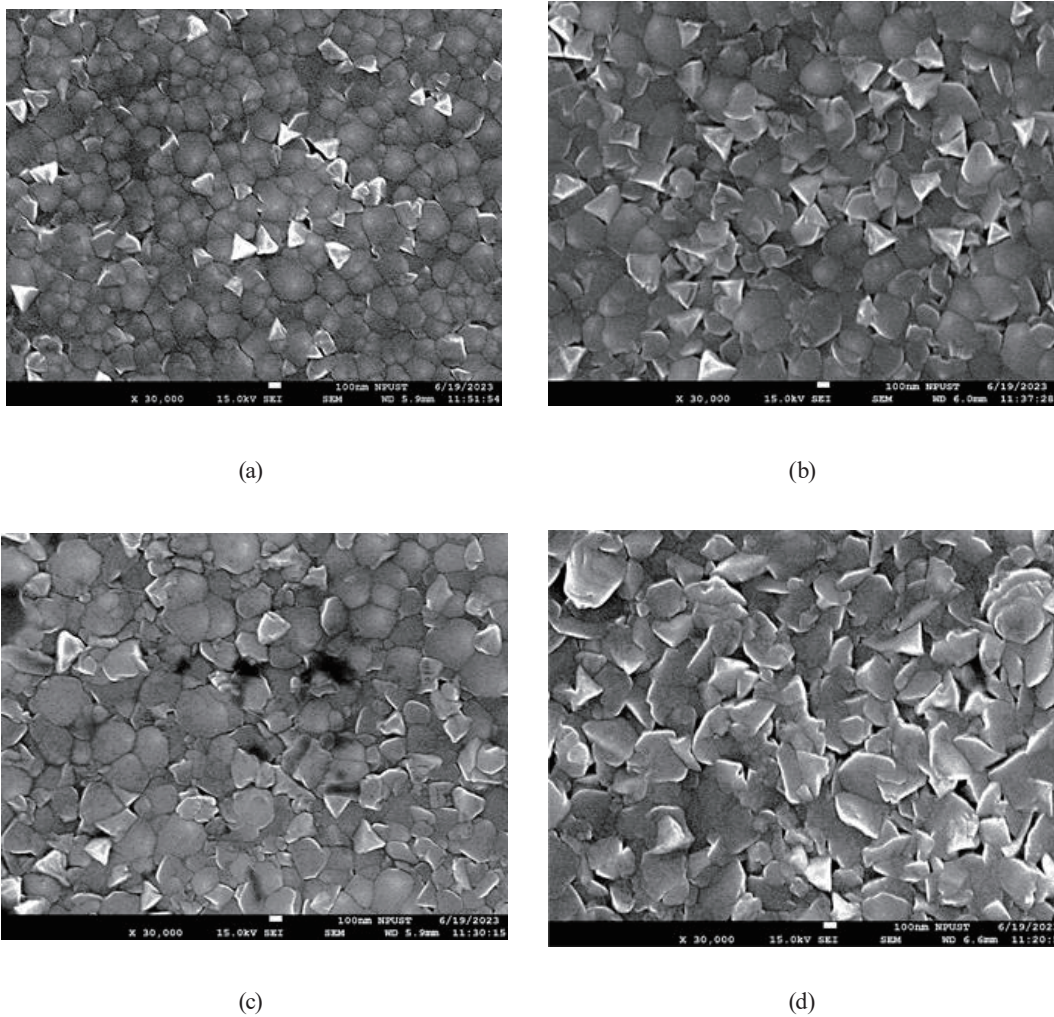

(a)

(b)

(c)

(d)

Fig. 9. SEM surface morphologies of ZnO films annealed for 4 h at different temperatures: (a) as-deposited, (b) 300, (c) 400, and (d) 500 ºC (magnification: ×30000).

the density of the lamellar structures increased [Fig. 9(c)]. However, although the overall grain size was larger than that of the sample annealed at 300 °C, no significant change occurred in the geometric structure of the grains. At the highest annealing temperature of 500 °C, the surface comprised a continuous and dense lamellar structure, as shown in Fig. 9(d). This observation is consistent with the XRD results presented in Fig. 8, which show that the maximum intensity of the (002) peak is obtained at 500 °C. A higher density of the lamellar structures is associated with an enhanced pyroelectric signal. Accordingly, the annealing temperature was set to 500 °C with a holding time of 4 h for all the remaining sputtering experiments.

Figure 10 shows the voltage responses of the sensors incorporating electrodes made of different materials. The electrode material had a significant effect on the sensor response. The electrode materials were ranked in descending order of their effects on the magnitude of the voltage response as follows: Ag > Au > Pt > Cu > Cr. The response voltage of the sensor fabricated with Ag electrodes was significantly higher than those of the other sensors. In particular, the maximum voltage magnitude (23.0 mV/mW at 60 Hz) was 4.1 times higher than the weakest signal produced by the Cr electrode (5.5 mV/mW) and 1.7 times higher than that of the commonly used Au electrode (12.2 mV/mW). As shown in Eqs. (2) and (3), the difference in the voltage response of the different sensors can be attributed directly to differences in the thermal conductivity coefficients of the sensor materials and the corresponding change in temperature-time change rate.

Figure 11(a) shows the voltage responses and t_{90} temperature-time change rates of the sensors patterned with different electrode materials. As shown, the sensors were ranked in terms of a decreasing voltage response and an increasing temperature-time change rate as follows: Ag, Au, Pt, Cu, and Cr. Figure 11(b) shows the thermal diffusivities and temperature-time response rates of the various electrodes. It is observed that the materials with a higher thermal diffusivity
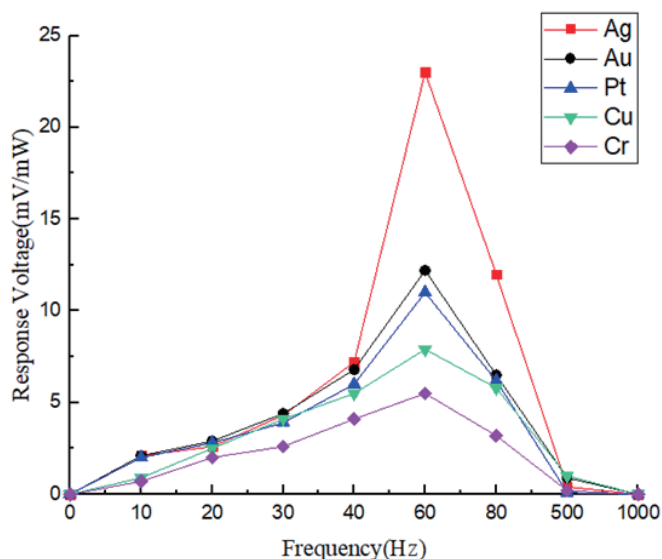

Fig. 10. (Color online) Variation in response voltage with excitation frequency as a function of electrode material. (Note that the grid side length is 200 μm and the number of electrode units is 256.) (Ag: 23.0 mV/mW @ 60 Hz; Au: 12.2 mV/mW @ 60 Hz ; Pt: 11.3 mV/mW @ 60 Hz ; Cu: 7.9 mV/mW @ 60 Hz ; Cr: 5.5 mV/mW @ 60 Hz)
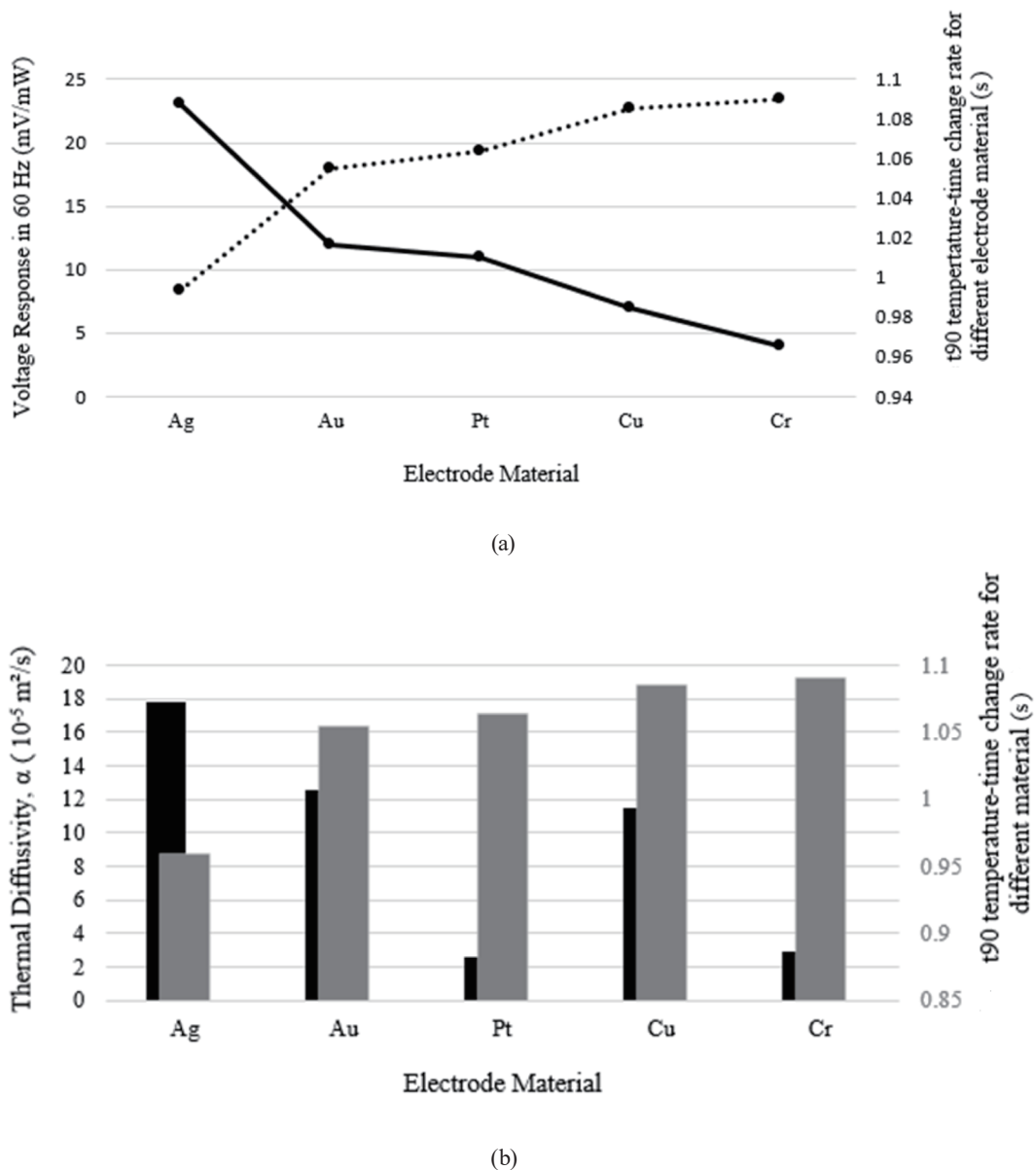
(a)

(b)

Fig. 11. (a) Voltage response at 60 Hz for different electrode materials (solid line) and t_{90} temperature-time change rates (dashed line). (b) Thermal diffusivities of different electrode materials (dark) and t_{90} temperature-time change rates (light).

generally resulted in a lower t_{90} time. For example, Ag had the highest thermal diffusivity (17.8×10^{-5} m^2/s) and the fastest t_{90} response (0.993 s). However, the Pt electrode was an exception to this trend. After annealing, the Cr and Cu electrodes underwent extensive oxidation that degraded their heat conduction performance. In contrast, the Pt electrode experienced a lower degree of oxidation owing to its superior anti-oxidation properties. Consequently, its thermal diffusivity properties were stabler under annealing than those of the Cr and Cu electrodes. Hence, even though the Pt electrode had the lowest thermal diffusivity among all the electrodes, its response was still faster than those of the Cr and Cu electrodes.

5. Conclusions

In this study, we investigated the IR sensing performance of five ZnO sensors fabricated using different electrode materials (Ag, Au, Pt, Cu, and Cr) and annealed at 500 ºC for 4 h. The experimental results showed that the sensor patterned with Ag electrodes yielded the maximum voltage response of 23 mV/mW owing to its superior thermal conductivity, whereas the Cr electrodes yielded the lowest voltage response of 5.5 mV/mW. In addition, the simulation results showed that in the upper region of the ZnO sensing layer, the time required to reach 90% of the final response when using the Ag electrodes was 9% shorter than that when using the Cr electrodes. Furthermore, in the lower region of the ZnO sensing layer, the Ag electrodes reduced the t_{90} time by 18% compared with the Cr electrodes. For all the electrode materials, the temperature-time change rate of the ZnO sensing layer was positively correlated with the response voltage. Finally, the temperature response of the lower region of the sensing layer was dominated by the material of the top electrode rather than the coverage of the sensing area.

References

1 D. Lienhard, S. Nitschke, B. Ploss, and W. Ruppl, W: Sens. Actuators, A **42** (1994) 553. https://doi.org/10.1016/0924-4247(94)80052-9
2 R. Takayama, Y. Tomita, J. Asayama, K. Nomura, and H. Ogawa: Sens. Actuators, A **22** (1990) 508. https://doi.org/10.1080/00150199108014770
3 C. C. Hsiao and S. Y. Yu: Sensors **12** (2012) 17007. https://doi.org/10.3390/s121217007
4 K. Hashimoto, M. Yoshinomoto, S. Matsueda, K. Morinaka, and N. Yoshiike: Sens. Actuators, A **58** (1997) 165. https://doi.org/10.1016/S0924-4247(97)01715-9
5 D. Lienhard, F. Heepmann, and B. Ploss: Microelectron. Eng. **29** (1995) 101. https://doi.org/10.1016/0167-9317(95)00124-7
6 C. C. Chang and C. S. Tang: Sens. Actuators, A **65** (1998) 171. https://doi.org/10.1016/S0924-4247(97)01663-4
7 J. S. Ko, W. Liu, and W. Zhu: Sens. Actuators, A **93** (2001) 117. https://doi.org/10.1007/s11706-007-0060-7
8 N. Chong, H. Chan, and C. Choy: Sens. Actuators, A **96** (2002) 231. https://doi.org/10.3390/s23156818
9 C. S. Wei, Y. Y. Lin, Y. C. Hu, C. W. Wu, C. K. Chih, C. T. Huang, and S. H. Chang: Sens. Actuators, A **128** (2006) 18. https://doi.org/10.3390/s121217007
10 C. C. Hsiao, Y. C. Hu, R. C. Chang, and C. K. Chao: Theor. Appl. Fract. Mech. **52** (2009) 1. https://doi.org/10.1016/j.tafmec.2009.06.002
11 C. C. Hsiao and S. Y. Yu: J. Mech. Sci. Technol. **25** (2011) 2835. https://doi.org/10.1007/s12206-011-0808-y
12 K. Cicek, T. Karacali, H. Efeoglu, and B. Cakmak: Sens. Actuators, A **260** (2010) 24. https://doi.org/10.1016/j.sna.2017.04.007
13 S. Gaur, K. Rangra, and D. Kumar: Sens. Actuators, A **300** (2019) 111660. https://doi.org/10.1016/j.sna.2019.111660
14 C. Y. Lee, C. X. Yu, K. Y. Lin, and L. M. Fu: Appl. Sci. **11** (2021) 9074. https://doi.org/10.3390/app11199074
15 B. Sharmila, K. Monoj, and D. Priyanka: Microelectron. J. **135** (2023) 105759. https://doi.org/10.1016/j.mejo.2023.105759
16 S. Bozoian, L. Kalaydjian, J. Younes, M. Tabbal, and M. Kazan: Infrared Phys. Technol. **128** (2023) 104519. https://doi.org/10.1016/j.infrared.2022.104519
17 R. W. Whatmore: Rep. Prog. Phys. **49** (1986) 1335. https://doi.org/10.1088/0034-4885/49/12/002